



Summary of Thesis

OPTICAL PROPERTIES OF RARE EARTH DOPED PEROVSKITE MATERIALS

*A THESIS
SUBMITTED BY*

VISHWNATHA RAJENDRAPRASAD VERMA

*FOR THE AWARD OF THE DEGREE OF
DOCTOR OF PHILOSOPHY*

IN
PHYSICS

UNDER THE GUIDANCE OF
Prof. M. SRINIVAS

**PHYSICS DEPARTMENT
FACULTY OF SCIENCE
THE MAHARAJA SAYAJIRAO UNIVERSITY OF BARODA
VADODARA
OCTOBER-2020**

Pure and rare earth doped pervoskite phosphor gathered scientific and technological important because of their luminescent, dielectric, semiconductor, catalytic, magnetic, fluorescent, and ion-exchange properties [1–3]. A large variety of properties and corresponding applications is the reason, why the synthesis of pervoskite is a more attractive field of research for researchers. Out of many properties, luminescent properties are significantly investigated by many researchers. Wide-bandgap rare-earth doped pervoskite phosphors have gained much more attention, for their potential applications in diverse areas such as X- and gamma-radiation detectors, lighting, display phosphors, light-emitting diodes, scintillators, and solid state lasers [4–6]. In this thesis, undoped, single Rare earth doped and double rare earth doped pervoskite phosphors are synthesis by hydrothermal method, solid state reaction method and combustion synthesis method to investigate its luminescence properties and its application.

The thesis comprises of seven chapters. **Chapter 1 (Introduction and Literature review)** comprises of the introduction to the research problem and its relevant literature review. **Chapter 2 (Experimental Method and Characterization Techniques)** contains the basic information of various synthesis method and the procedure followed for the synthesis of phosphors. This chapter also contain information related to characterization techniques. **Chapter 3 (Synthesis and Characterization of Strontium Cerium Niobate Nanophosphor)** in this chapter, synthesis method and characterization of strontium cerium niobate oxide was explained in detail. The result of characterization was also discuss in detail with require graphs and images. **Chapter 4 (Synthesis and Photoluminescence studies of undoped and doped Strontium Gadolinium Tantalum Oxide)** in this chapter, synthesis method and characterization of undoped and doped strontium gadolinium tantalum oxide was explained in detail. The result of characterization was also discuss in detail with require graphs and images. **Chapter 5(Photoluminescence Studies of Strontium Gadolinium Niobate Oxide)** in this chapter, synthesis method and characterization of strontium gadolinium niobate oxide was explained in detail. The result of characterization was also discuss in detail with require graphs and images. **Chapter 6 (Synthesis and Photoluminescence studies of undoped and doped Barium Cerium Niobate Oxide)** in this chapter, synthesis method and characterization of undoped and doped barium cerium niobate oxide was explained in detail. The result of characterization was also discuss in

detail with require graphs and images. **Chapter 7 (Conclusion)** in this chapter, outcome of all prepared phosphors are explained in detail.

Chapter 1: Introduction

Various kinds of luminescence emission are observed in nature such as lightening, aurora, fireflies, etc. The luminescence emission from the sea bacteria were observed by the ancient Chinese (1500-1000 B.C.). The information regarding to the knowledge of luminescence in India is found in holy writings of ancient India - the Vedas. Aristotle (384-382 B.C.) from Greece had observed light being emitted from decaying fish [7].

In 1888, the German physicist Eilhardt Wiedemann first introduced the word luminescence to include both phosphorescence and fluorescence [8-12]. In Latin, a word '*lumen*' means '*light*' from where the word luminescence originated. Nowadays, the word luminescence is defined as a phenomenon in which the electronic state of a luminescent substance is excited by some kind of external energy given to the substance [13].

The pervoskite mineral was discovered in the Ural Mountains of Russia by Gustav Rose in 1839 and is named after Russian mineralogist Lev Perovski (1792–1856). In pervoskite, a divalent cation is consolidated with a quadrivalent cation. Within certain limits of cation size, different combinations of a divalent and a quadrivalent cation have the pervoskite structure with differing degrees of distortion from the ideal cubic form [14–16]. Moreover, within certain cation-size limitations, other cation combinations with a total charge of six can proxy for the A^{2+} : B^{4+} combination. For example, lanthanum aluminate oxide ($LaAlO_3$) both are trivalent while in $KNbO_3$ (potassium niobate) have a monovalent and a pentavalent cation has the pervoskite structure [4, 17]. In the case of double pervoskites such as $A_2B_2O_6$, stoichiometric control of two cations at the B site is known to be advantageous for visible light photocatalysis.

Compounds with general formula $A_2B_2O_6$ belong to the double pervoskites and they have similar crystal structures as simple pervoskites. Double pervoskites have the basic structure of corner connected BO_6 octahedra and A cations enclosed inside. However, the connectivity of the octahedra may alter from structure to structure. Double pervoskites could contain different cations at the A or/and B sites, using a general form $AA'BB'O_6$ [18, 19].

Chapter 2: Experimental Methods and Characterization Techniques

The perovskite phosphors present in this thesis are prepared by various methods. These phosphors are synthesized by hydrothermal method, solid state reaction method and combustion synthesis method. In hydrothermal process, an aqueous mixture of reagents prepared from their stoichiometric ratio obtained through the chemical reaction is heated at a constant temperature in an airtight stainless steel shell (autoclave) [20]. The temperature of the autoclave had been raised above the steaming temperature of the water which could be maintained at a constant value $< 300^{\circ}\text{C}$ for 10-24 hours depends on the reaction. However the volume of the autoclave is constant, consequently, the temperature above the boiling point of water increases the pressure within the reaction autoclave which is intensely increased beyond atmospheric pressure. The combined effect of high temperature and pressure in this method provides an extensive single-step chemical process to produce highly crystalline material which could not require post-annealing treatments to obtain pure material [21, 22].

Reactions between or within solid reactants to yield a solid product are prototypical of solvent free reactions [23]. From literature reports the concept of chemical reactivity between solids (and very often within solids) is very difficult to define [24]. The confined environment of the reactant crystal lattice can control the kinetic features of a reaction and hence the nature of products. Such reactions are said to be topochemically controlled and illustrate the topochemical principle proposed by Cohen and Schmidt in which reactions in the solid state take place with minimum requirements of energy and atomic or molecular motion requirements [25, 26].

Combustion synthesis method generally called as self-propagating high-temperature synthesis, was discovered in the 1980s. Combustion synthesis method was accidentally discovered by Prof. Patil in his laboratory in India in 1988 [27]. It is mainly a wet-chemical processing method. It does not require additional calcination of the material and repetitive heating treatment. Combustion synthesis method is an efficient and inexpensive method for the production of highly crystalline materials like inorganic-ceramic phosphor, magnetic materials, etc [28]. It is an extensively useful method to develop materials in all sections for commercial and industrial applications. It is one of the most popular methods that draw attention from the scientists and material technologists of various disciplines since last three decades. The physical properties like structure having crystalline or amorphous, purity of

material, surface area, particle size, porosity and agglomeration of the synthesized powders which highly depends on the parameters adopted for the process [29]. All these phosphors are characterized by X-ray diffraction, FTIR, SEM and Photoluminescence.

Chapter 3: Synthesis and Photoluminescence studies of Strontium Cerium Niobate Nanophosphor

Strontium Cerium Niobate synthesis by hydrothermal method and characterized by XRD, FTIR, SEM and Photoluminescence.

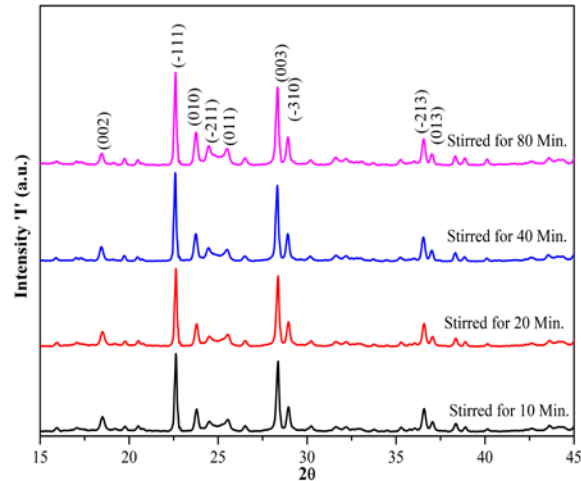


Figure 1 X-Ray Diffraction patterns of Sr₂CeNbO₆ phosphors.

Figure 1 presents the X-ray diffraction (XRD) pattern of Sr₂CeNbO₆. As stirring time increased, the intensity and crystallinity of Sr₂CeNbO₆ also increased. The phosphors that have high crystallinity always means few defects and also have stronger luminescence [30]. All the reflection peaks of the X-ray profile are indexed, and lattice parameters are determined with the help of a standard computer program Powder – X. Inter-planer spacing (d-spacing) suggests that all phosphors have a monoclinic structure with space group P2₁/n at room temperature [31, 32]. Average crystalline size of all sample are calculated by using Scherrer formula which was given below [33].

$$D = \frac{k \cdot \lambda}{\beta \cdot \cos \theta} \dots \dots \dots (1)$$

Where, λ = wavelength of X-ray i.e. 1.5443 Å, θ = Diffraction angle, k = constant 0.94 and β = FWHM.

The broadening effect of XRD peaks reflects the nano crystalline nature of the resulting Sr₂CeNbO₆ samples. Since the effective XRD peak broadening can be caused by lattice strain and small crystallite size, these two effects have to be distinguished. This

can be calculated by plotting $\beta \cos\theta$ versus $\epsilon \sin\theta$ in the following relation (Williamson–Hall plot) [33].

$$\beta_{hkl} * \cos\theta_{hkl} = \left(\frac{k*\lambda}{D}\right) + \epsilon * \sin\theta_{hkl} \dots\dots\dots (2)$$

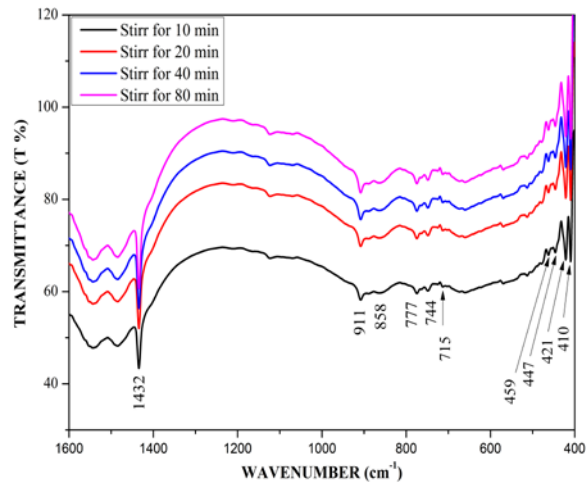
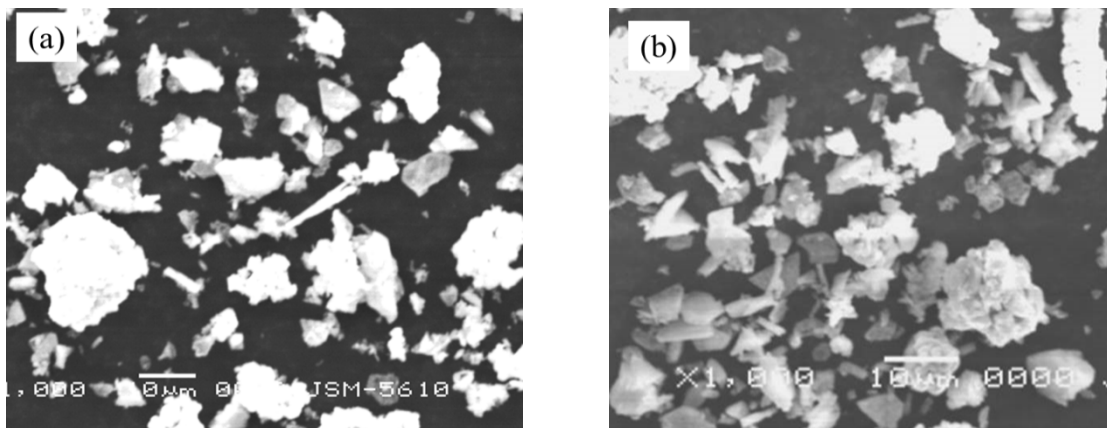


Figure 2 FTIR spectra of Sr₂CeNbO₆ phosphors.

Figure 2 shows FTIR spectra of Sr₂CeNbO₆ with a range of wavenumber from 400 cm⁻¹ to 1600 cm⁻¹. The IR spectrum of Sr₂CeNbO₆ shows some well-defined bands in Figure 2. This is in good accordance with what is systematically found for a perovskite structure following group theory prophecies [34]. The observed shoulder peak at 715 cm⁻¹ recommends the overlapping of Sr₂O₆ and NbO₆ stretching bands with the displacement toward higher frequencies of the NbO₆ bands [35].



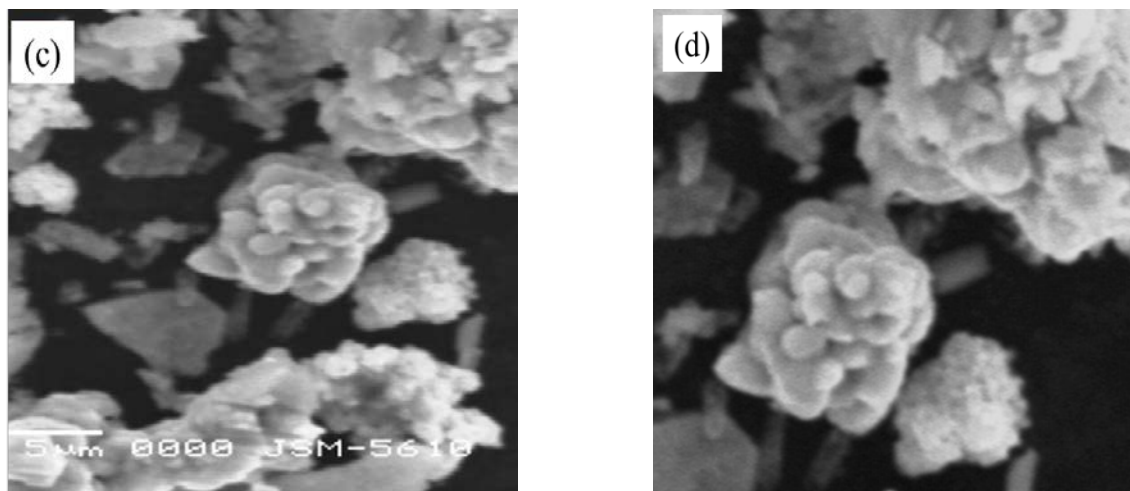


Figure 3 (a), (b), (c), and (d) SEM image of $\text{Sr}_2\text{CeNbO}_6$ phosphors for 10 min., 20 min., 40 min., and 80 min. stirring time respectively.

Figure 3 (a) shows particles of SCN producing numerous types of shapes like hexagonal, needle, flowered, etc. This different variety of shapes is uniquely obtained. As the stirring time increases, the shape of SCN particles becomes unique, but the size of the particle also differs as shown in Figure 3 (b). As stirring time increases at room temperature, cotton flower type shape occurred, which presented in Figure 3(c) and (d).

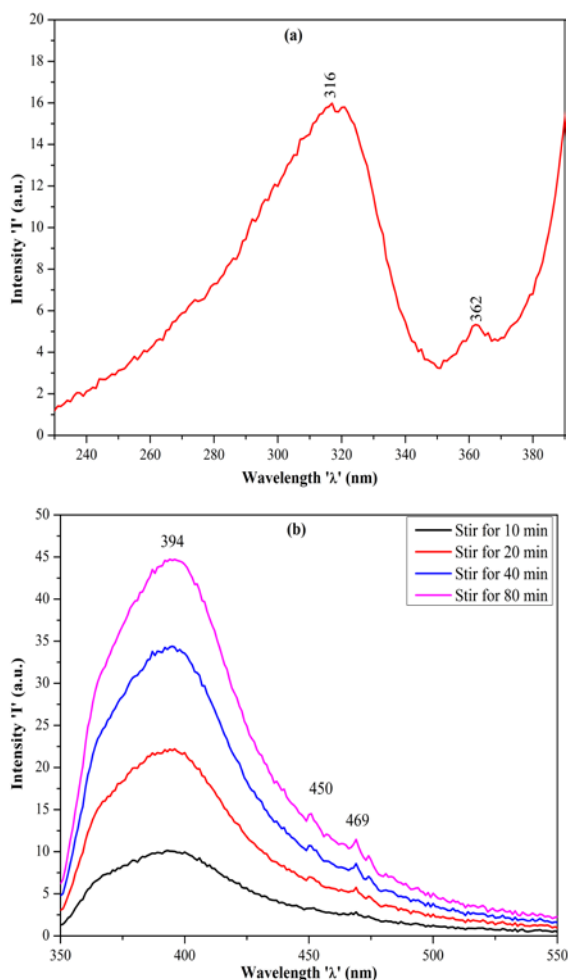


Figure 4 (a) Excitation spectra of Sr₂CeNbO₆ and (b) Emission spectra of Sr₂CeNbO₆.

Figure 4 shows the PLE and PL spectra were recorded at room temperature of Strontium Ceria Niobate (SCN). A broad emission band occurred corresponding to the parity-allowed electric dipole transition ($5d \rightarrow 4f$). The emission spectra were compounded by broad and asymmetric band emission centered at about 394 nm attributed to the transition, from the lowest of the crystal field component of $5d^1$ to the two levels of the ground state $^2F_{5/2}$ and $^2F_{7/2}$ [36].

The emission spectra show two shoulder peaks at 450nm and at 469nm with energies 2.75eV and 2.645eV respectively. As the stirring time increased the shoulder peaks generated prominently the optical transitions that occurred in Ce^{+3} from $5d$ to $4f$, which are relatively fast (~ 20 – 40 ns).

Chapter 4: Photoluminescence studies of Europium doped Strontium Gadolinium Niobate Oxide

Strontium Gadolinium Niobate synthesis by Solid State Reaction method and characterizes by XRD, FTIR, and Photoluminescence.

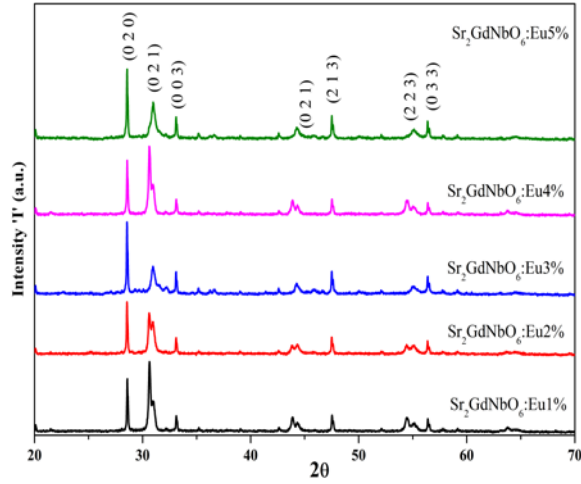


Figure 5 X-ray diffraction pattern of Eu(III) doped $\text{Sr}_2\text{GdNbO}_6$.

Figure 5 presents the X-ray diffraction (XRD) pattern of $\text{Sr}_2\text{GdNbO}_6$. As stirring time increased, the intensity and crystallinity of $\text{Sr}_2\text{GdNbO}_6$ also increased. The phosphors that have high crystallinity always means few defects and also have stronger luminescence [30]. All the reflection peaks of the X-ray profile are indexed, and lattice parameters are determined with the help of a standard computer program Powder – X. Inter-planer spacing (d-spacing) suggests that all phosphors have a monoclinic structure with space group $P2_1/n$ (#014) at room temperature [31, 32]. Average crystalline size of all sample are calculated by using Scherrer formula which was given below [33].

$$D = \frac{k \cdot \lambda}{\beta \cdot \cos \theta} \dots \dots \dots (1)$$

Where, λ = wavelength of X-ray i.e. 1.5443 \AA , θ = Diffraction angle, k = constant 0.94 and β = FWHM.

In double perovskite oxide, the study of distortion from the ideal cubic perovskite structure is clear as the $\text{Sr}_2\text{GdNbO}_6$ complex perovskite has the general formula $A_2\text{BB}'\text{O}_6$. The tolerance factor T_f [37] of the sample is calculated by using equation (2),

$$T_f = \frac{R_{\text{Sr}} + R_{\text{O}}}{\sqrt{2} \left(\frac{R_{\text{Gd}} + R_{\text{Nb}}}{2} + R_{\text{O}} \right)} \dots \dots \dots (2)$$

Where, R_{Ba} , R_{Ce} , R_{Nb} and R_{O} are the ionic radii of Sr, Gd, Nb and O respectively [38]. By the geometry of crystal, the ideal cubic structure should have $T_f = 1$, whereas it will be monoclinic structure for values of $T_f < 1$ and it following the SPuDs prediction [39]. The value of tolerance factor for $\text{Sr}_2\text{GdNbO}_6$ was found to be approximately 0.9218, which suggests that sample under study has the monoclinic structure.

The broadening effect of XRD peaks reflects the nano crystalline nature of the resulting Sr₂GdNbO₆ samples. Since the effective XRD peak broadening can be caused by lattice strain and small crystallite size, these two effects have to be distinguished. This can be calculated by plotting $\beta \cos\theta$ versus $\epsilon \sin\theta$ in the following relation (Williamson–Hall plot) [33].

$$\beta_{hkl} * \cos\theta_{hkl} = \left(\frac{k*\lambda}{D}\right) + \epsilon * \sin\theta_{hkl} \dots\dots\dots (2)$$

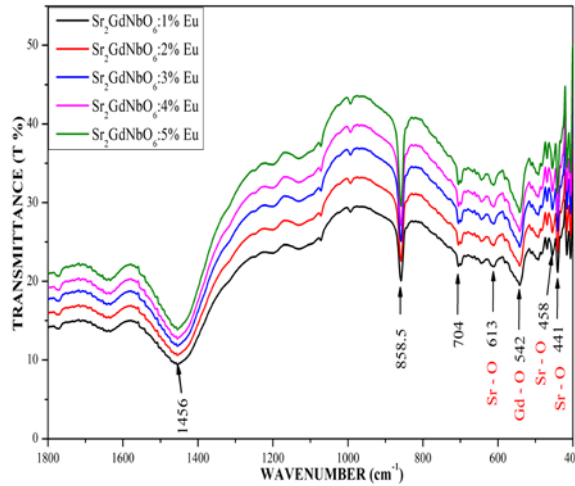


Figure 6 FTIR spectra of Eu(III) doped Sr₂GdNbO₆.

In Figure 6 FTIR spectra of Sr₂GdNbO₆ has shown with a range of 400 cm⁻¹ to 1800 cm⁻¹ wavenumber. The FTIR spectrum of Sr₂GdNbO₆ shows some well-defined bands in the figure 6 It is in good accordance with what orderly found for a pervoskite type structure following group theory predictions [34]. The bands at 542 cm⁻¹ are assigned to the Gd-O vibration. [40–42]. The symmetric stretching vibrations from 838.8 cm⁻¹ completely support the possible presence of edge-connected Nb-O octahedra.

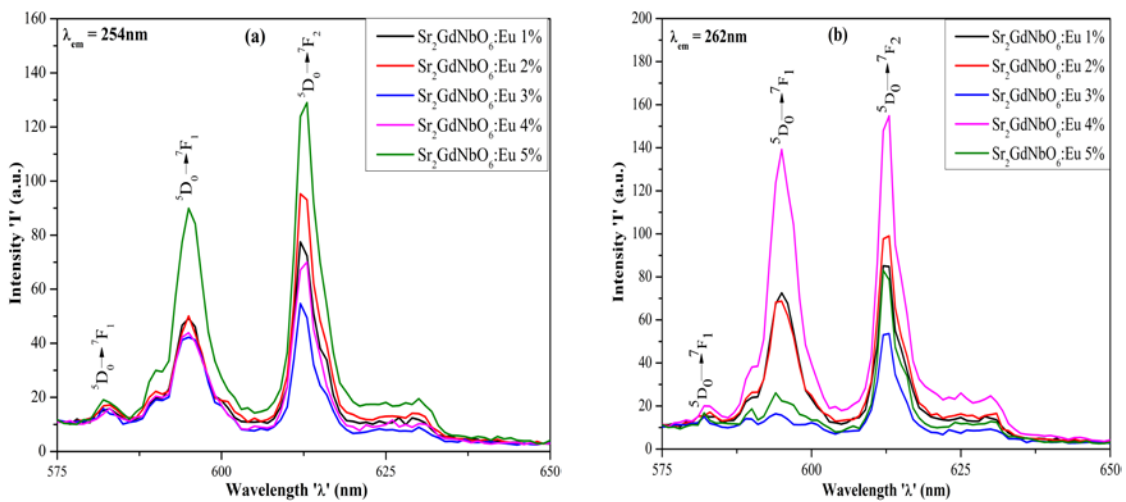


Figure 7 Photoluminescence emission spectra of Eu(III) doped Sr₂GdNbO₆ (a) excitation wavelength 254nm, and (b) excitation wavelength 262nm.

The Eu(III) doped Sr₂GdNbO₆ samples exhibit three visible emission bands around 582, 596, and 613 nm. These assigned to the magnetic dipole (MD) and electric dipole (ED) transitions of europium ⁵D₀ → ⁷F₁, ⁵D₀ - ⁷F₂. The emission of Eu(III) has assigned to transition from the ⁵D₁ and ⁵D₀ levels to the ⁷F_J (J = 0 – 6) levels [43].

The site symmetry of Eu³⁺ ion in the host lattice can be predicted by asymmetry ratio, which can be defined by equation (4),

$$\text{asymmetry - ratio} = \frac{I(5D_0 \rightarrow 7F_2)}{I(5D_0 \rightarrow 7F_1)} \text{----- (4)}$$

Where, I (⁵D₀→⁷F₂) and I (⁵D₀→⁷F₁) are the intensities of electric dipole and magnetic dipole transition peaks, respectively. If the asymmetry ratio is more than one, then Eu(III) substituted at the non-centrosymmetric site. For the asymmetric proportion less than 1, Eu(III) placed at a centrosymmetric position in the host lattice. Here, the asymmetry ratio found to be more than 1, so the phosphor shows that Eu(III) placed at A site in the host lattice and is in good agreement with the presently reports [44–49]. It is good to point out that the incorporation of the emission color corresponding to coordinate points yields a mixture of light with color in the orange-red region possess glow correlated color temperature, i.e., CCT in the 1700K – 2500K range.

Chapter 5: Synthesis and Photoluminescence studies of undoped and Europium doped Barium Cerium Niobate Oxide

Barium Cerium Niobate synthesis by combustion method and characterizes by XRD, FTIR, and Photoluminescence.

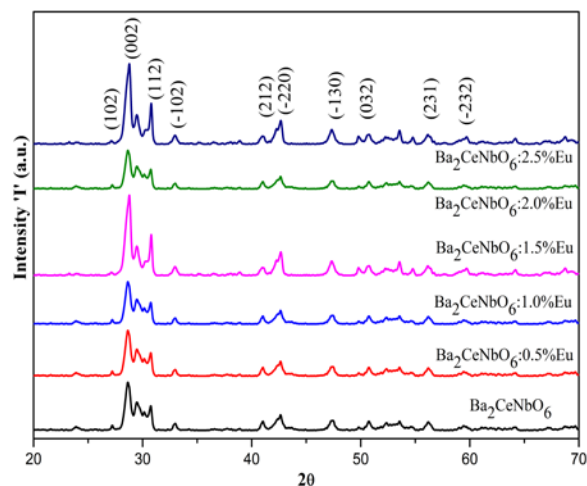


Figure - 8 X-ray diffraction pattern of undoped and Eu(III) doped $\text{Ba}_2\text{CeNbO}_6$.

These diffraction lines are consistent and confirm the formation of a double perovskite structure for all studied samples. The average crystallite sizes were estimated by the Scherrer's equation using the full width at half maximum (FWHM) of all intense peak [50]. All the reflection peaks of the X-ray profile indexed and lattice parameters are determined with the help of a standard computer program Powder-X. The value of tolerance factor for $\text{Ba}_2\text{CeNbO}_6$ was found to be approximately 0.9505, which suggests that sample under study has the monoclinic structure [51]. The broadening effect of XRD peaks reflects the nanocrystalline nature of the resulting Eu(III) doped $\text{Ba}_2\text{CeNbO}_6$ samples. Since the effective XRD peak broadening can be caused by lattice strain and small crystallite size, these two effects have to be distinguished.

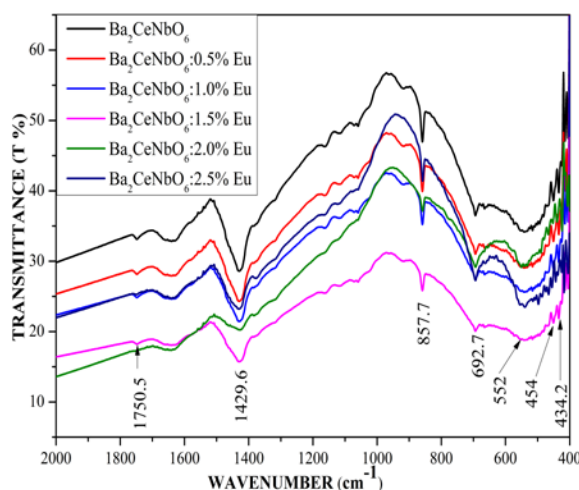


Figure 9 FTIR spectra of undoped and Eu(III) doped $\text{Ba}_2\text{CeNbO}_6$.

The FTIR spectrum of $\text{Ba}_2\text{CeNbO}_6$ shows some well-defined bands in the above figure. It is in good accordance with group theory predictions what orderly found for perovskite type structures [34]. All the peaks in the spectra are typical of the material. One small hump is at 1750 cm^{-1} , which is due to the presence of adsorbed moisture in KBr [52]. The lower energy band found at around $450\text{--}650\text{ cm}^{-1}$ is related to the deformational mode of CeO_6 octahedra [53]. The medium energy peak appearing near 850 cm^{-1} is due to the asymmetric NbO_6 stretching vibration [54] due to the higher charge of the cation. The peak at 552 cm^{-1} is due to the Ba-O.

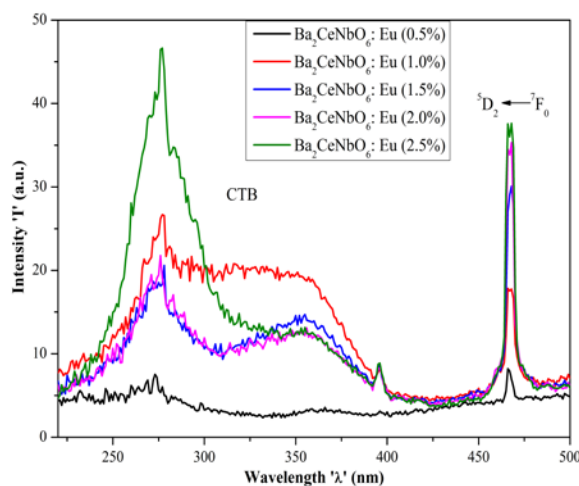


Figure 10 Photoluminescence Excitation spectra of Eu(III) doped Ba₂CeNbO₆.

Figure 10 represents the absorption spectra of Eu(III) doped Ba₂CeNbO₆ phosphor. These excitation spectra recorded with the 613nm emission wavelength. An intense peak at 466 nm wavelength is due to the ${}^5D_2 \leftarrow {}^7F_0$ electric dipole transition [55]. The absorption spectra of Eu(III) compounds allows the determination of higher energy levels of the $4f_6$ electronic configuration of Eu³⁺ ion. The transitions to the 5D_0 , 5D_1 , and 5D_2 levels were called the yellow, green and blue bands based on their places in the visible spectrum [56, 57]. The transitions of ${}^5D_0 \leftarrow {}^7F_1$ and ${}^5D_0 \leftarrow {}^7F_2$ are suitable for determining the location of the 5D_0 level if the ${}^5D_0 \leftarrow {}^7F_0$ transition is forbidden.

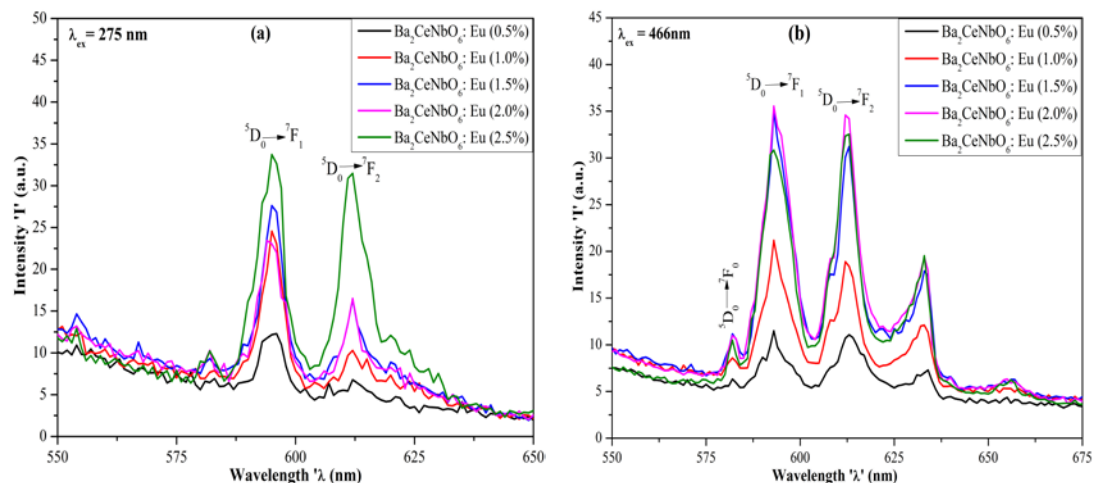


Figure 11 Photoluminescence emission spectra of Eu(III) doped Ba₂CeNbO₆ (a) excitation wavelength 275nm and (b) excitation wavelength 466nm.

Fig. 11 (a) and (b) depict typical PL emission spectra of Eu (III) doped Ba₂CeNbO₆ phosphors excited with 275nm and 466nm wavelength. In the present study, the concentration of europium ranges from 0.5 to 2.5 mole percentage. The Eu (III) doped Ba₂CeNbO₆ phosphors exhibit two visible emission bands around 596 and 613 nm

when excited at 275nm while it displays four emission peaks at 582nm, 596nm, 613nm, and 633nm. These emission peaks are assigned to the magnetic dipole (MD) ${}^5D_0 \rightarrow {}^7F_1$ and electric dipole (ED) ${}^5D_0 \rightarrow {}^7F_2$ transitions of europium when excited with 275nm and 466nm. The emission peak at 596 nm is due to the magnetic dipole transition of ${}^5D_0 \rightarrow {}^7F_1$, which has higher intensity compare to peak at 613nm of ${}^5D_0 \rightarrow {}^7F_2$ electric dipole transition during excitation at 275nm. This asymmetricity confirms that the Eu^{3+} ions are located at the non-inversion symmetric sites in host material [58–60].

It's important to note that in both the emission spectra emission peak at around 613nm is occurred in the red region. In emission spectra peak at 633nm seen when phosphor excited at 466nm wavelength, which is attributed due to ${}^5D_0 \rightarrow {}^7F_2$ electric dipole transition. Though an admixture of odd-parity electronic configuration to the pure 4f (like a non-centrosymmetric crystal field component) [61, 62] will allow the ED transitions partially and their possibility of occurrence is much higher than the probability of parity-allowed magnetic dipole (MD) (${}^5D_0 \rightarrow {}^7F_1$) transition. The asymmetric ratio is found to be less than unity (1), indicates that Eu (III) is substituted at a non-centrosymmetric site in the host lattice.

Chapter 6: Synthesis and Photoluminescence studies of undoped, single doped and double doped Strontium Gadolinium Tantalum Oxide

Strontium Gadolinium Tantalum oxide synthesis by combustion method and characterizes by XRD, FTIR, and Photoluminescence.

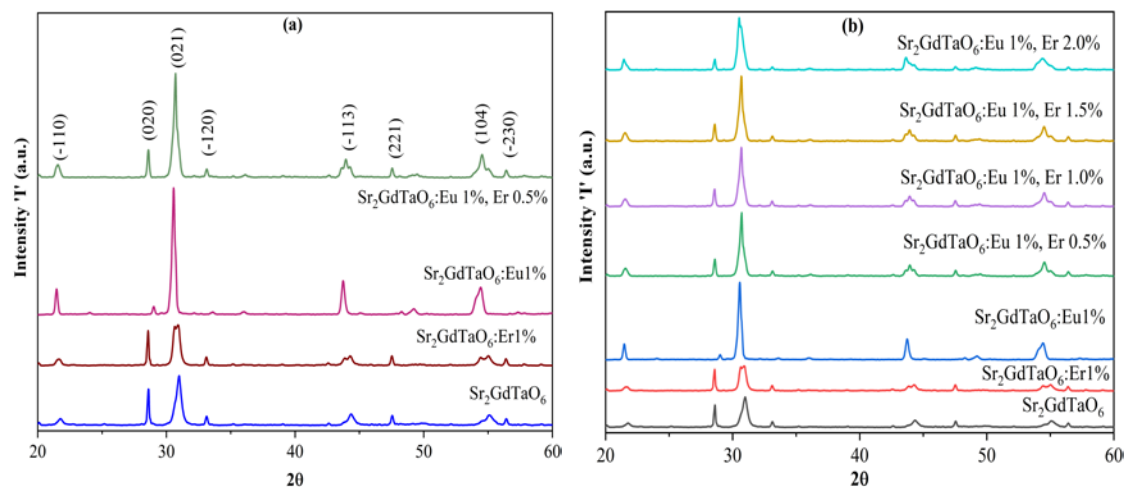


Figure 12 Powder X-ray diffraction pattern of (a) undoped, single doped, double doped $\text{Sr}_2\text{GdTaO}_6$ and (b) Eu(III), Er(III) double doped $\text{Sr}_2\text{GdTaO}_6$.

Figure 12 exhibits the powder X-ray diffraction pattern of undoped, single doped, and Eu(III), Er (III) double doped $\text{Sr}_2\text{GdTaO}_6$. The recorded patterns present sharp and

well-defined peaks, indicating that the as prepared materials have a highly crystalline nature. There is a good agreement between the observed and calculated interplanar spacing (d-values) that suggest, the compound has a monoclinic phase with a $P2_1/n$ (#14) space group [31]. The average crystallite sizes were estimated by the Scherrer's equation using the full width at half maximum (FWHM) of all hkl marked intense peak. The average crystallite size calculated using the Debye-Scherrer formula[33], which is given as equation (1),

$$D = \frac{k \cdot \lambda}{\beta \cdot \cos\theta} \quad \text{-----} \quad (1)$$

Where, D is the average crystallite size, k is the constant equal to 0.94, λ is the wavelength of the X-rays equal to 0.1542 nm, θ is the Bragg angle and β is FWHM.

The malformation from the ideal cubic perovskite the structure is an outcome of the inclination of the $Gd-O_{6/2}$ and $Ta-O_{6/2}$ octahedra; in the meantime support their corner connectivity. Then, the Ta^{5+} and Gd^{3+} cations occupy two crystallographic independent octahedral sites, namely 2d and 2c [63]. The crystallographic results of all prepared perovskite are in accordance with other reports, but there is no an enhanced characterization about atomic positions and inter-atomic distances [64].

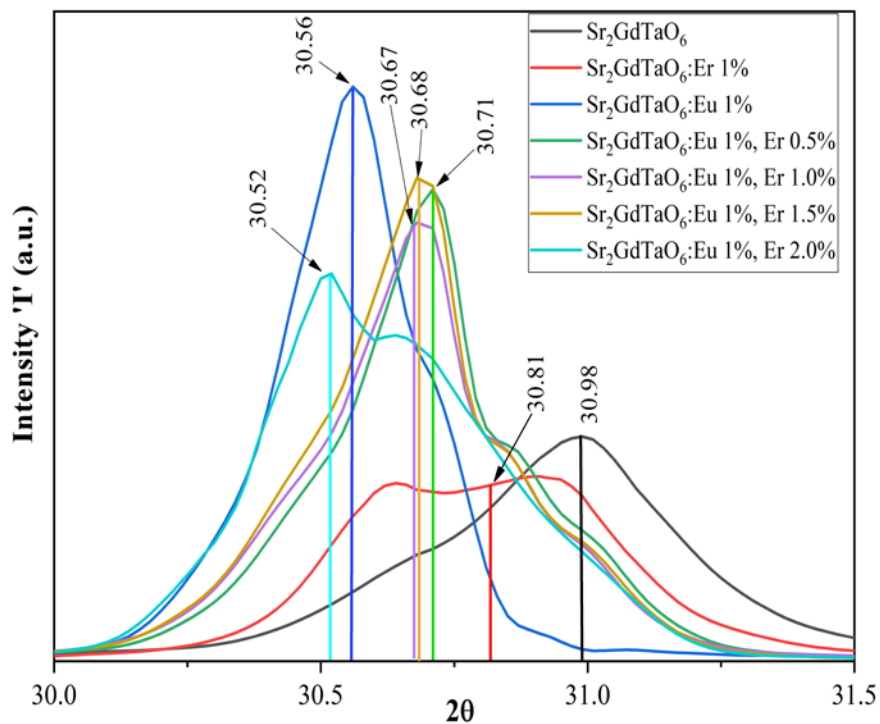


Figure 13 Magnified (021) reflection peak of undoped, single doped and Eu(III), Er(III) double doped Sr_2GdTaO_6 .

From Bragg's equation, the variation in position of reflection peaks implies the change in the lattice parameter of synthesized phosphors [33, 38]. To confirm the change

in reflection peaks, the magnified scale of characteristic reflection peak (021) of all $\text{Sr}_2\text{GdTaO}_6$ samples as seen in Figure 13. Due to small crystallite size, the number of parallel planes available is too small for a sharp diffraction maximum to build up and hence the reflection peaks in the diffraction pattern become broadened for all samples (Figure 13)[66].

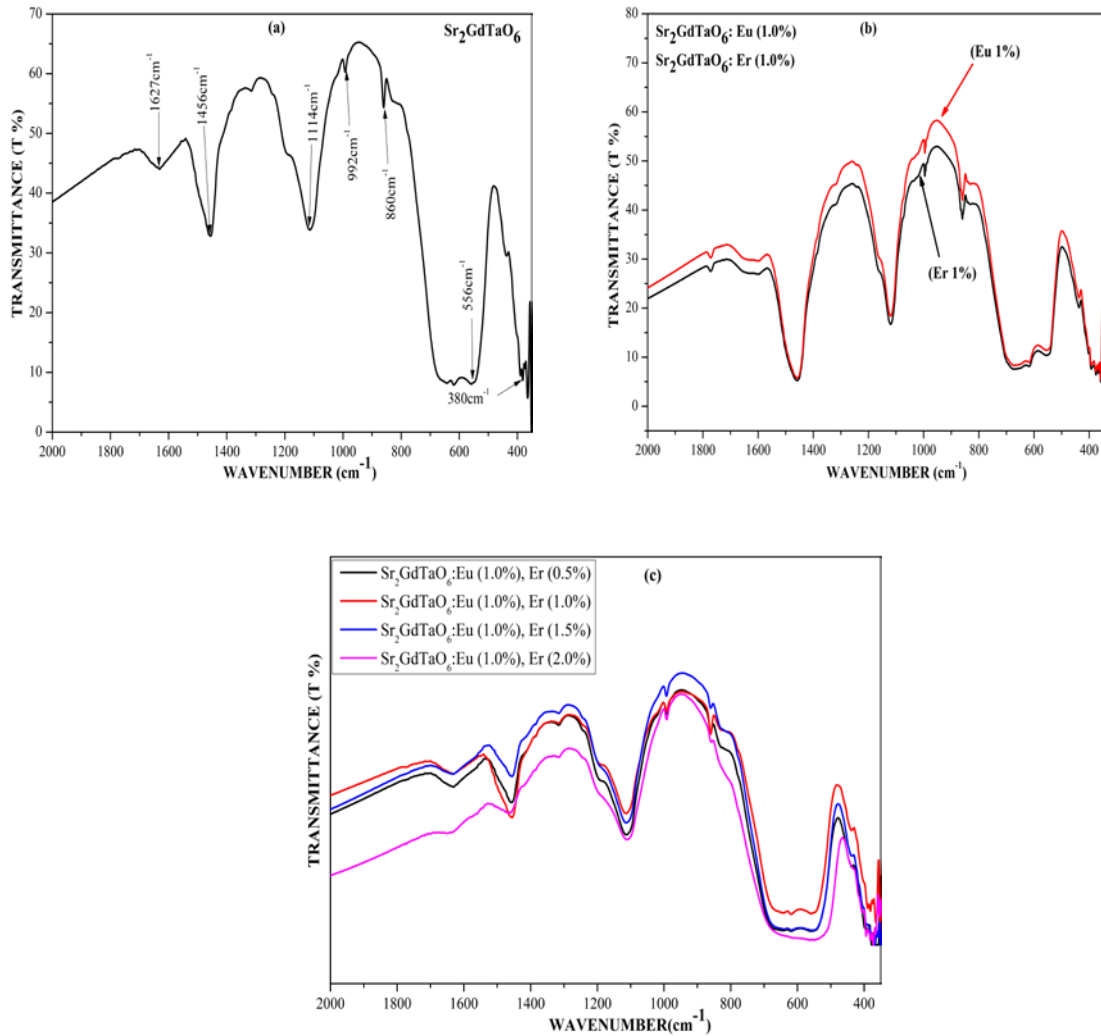


Figure - 14 FTIR spectra of (a) Undoped $\text{Sr}_2\text{GdTaO}_6$ and (b) single doped $\text{Sr}_2\text{GdTaO}_6$ and (c) Eu(III), Er(III) double doped $\text{Sr}_2\text{GdTaO}_6$

Figure 14 (a-c) exhibits the FTIR transmission pattern of undoped, single doped, and Eu(III), Er(III) double doped $\text{Sr}_2\text{GdTaO}_6$. The FTIR spectra were recorded via the potassium bromide (KBr) pellet structure using the pellet technique. The infrared pattern presents three well-defined bands at 380 cm^{-1} , 566 cm^{-1} , and 1456 cm^{-1} . The energy band at 380 cm^{-1} is due to the asymmetric bending of the TaO_6 octahedra while the strong energy band at 566 cm^{-1} attributed to the asymmetric stretching of the TaO_6 octahedra [67]. Perovskite type materials usually present characteristic two band spectra dominated by the antisymmetric F_{10} stretching and deformation modes of the MO_6 octahedra [43–

46]. The weak band at around 1456 cm^{-1} likely corresponds to the overtones of the fundamental vibrations in undoped, single doped, and Eu(III), Er (III) double doped $\text{Sr}_2\text{GdTaO}_6$. A very small peak at 1627 cm^{-1} is of the carrier $\text{KBr}\cdot(\text{H}_2\text{O})_n$ [31]. The absorption peaks at 992 cm^{-1} and 860 cm^{-1} due to legend formation were assigned to stretching characteristics of SrCO_3 [72].

There has been a long-running dispute about the nature of PL appearance in perovskites. Lots of experiments have been performed at room temperature as well as at the low temperature in many perovskites to explain PL behavior [82, 86, 89, 93, 94]. The development of room-temperature PL emission in amorphous type perovskite encourages notable research interests for room temperature PL of perovskite materials.

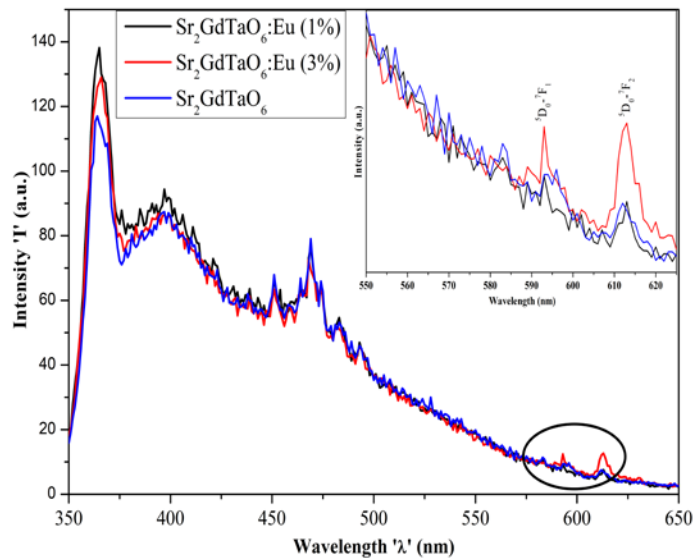


Figure 15 PL spectra of $\text{Sr}_2\text{GdTaO}_6$, $\text{Sr}_2\text{GdTaO}_6:\text{Eu}$ (1%) and $\text{Sr}_2\text{GdTaO}_6:\text{Eu}$ (3%)

Figure 15 exhibits photoluminescence spectra of undoped and Eu(III) doped $\text{Sr}_2\text{GdTaO}_6$. A magnified portion from 575nm to 625nm of PL of undoped and 1% Eu^{3+} doped $\text{Sr}_2\text{GdTaO}_6$ displayed in inset figure. In the magnified portion, there is a small effect of Eu^{3+} in the PL spectra of $\text{Sr}_2\text{GdTaO}_6$. Limited number of PL emission of Eu^{3+} maybe due to crystal field quenching effect observed in emission spectra of $\text{Sr}_2\text{GdTaO}_6$.

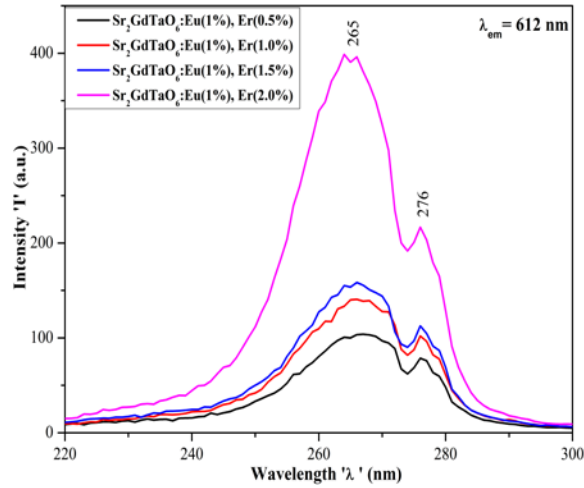


Figure 16 Photoluminescence excitation spectra of Eu(III), Er(III) double doped Sr₂GdTaO₆.

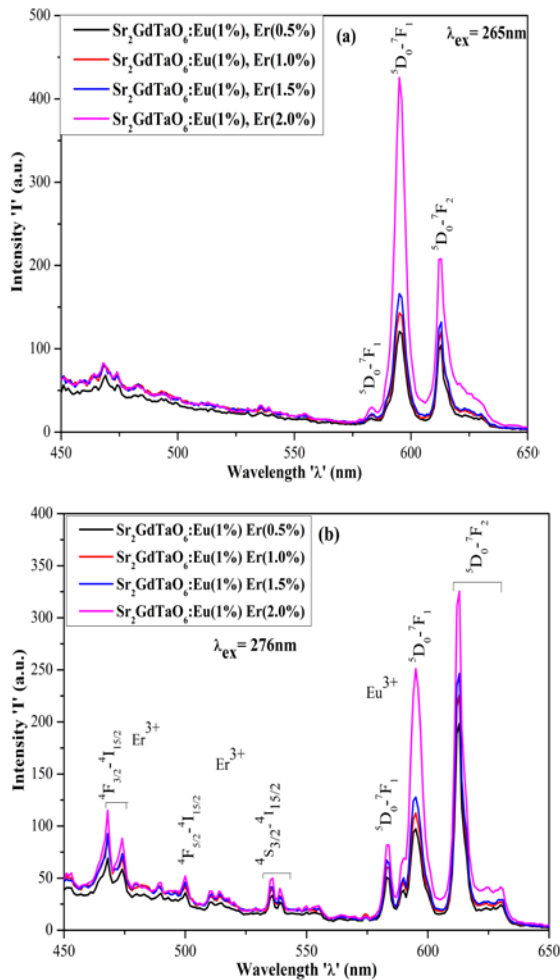


Figure 17 Photoluminescence spectra of Eu(III), Er(III) double doped Sr₂GdTaO₆ of excitation wavelength (a) 265nm and (b) 276nm.

Figure 16 shows room-temperature photoluminescence excitation spectra at 616nm. This PLE spectrum shows broad band with peak at 265nm and 276nm from the

intra configuration of the 4f–4f transitions of Eu^{3+} . The broad band peaking at 265 nm can be ascribed to the charge transfer (CT) transition of the filled 2p orbitals of O^{2-} ions to the partially filled 4f orbitals of Eu^{3+} ions when in the octahedral field, of which the position is mainly determined by the Eu – O distance [77]. When smaller Eu^{3+} ions substitute the Sr^{2+} sites, the lattice shrinks and the Eu – O bond becomes shorter and stronger, which will take more energy to break, thus a blue shift of CT band emerge [78, 79].

Figure 17 (a & b) displays typical emission spectra of radiation emanating from the Eu(III), Er (III) double doped $\text{Sr}_2\text{GdTaO}_6$ phosphors excited at 265nm and 276nm with a fixed europium concentration of 1.0mol% and increasing erbium concentration from 0.5 to 2.0mol% with an increment of 0.5 mol%. These phosphors were excited using xenon lamp operated at a 265nm and 276nm. The Eu(III), Er (III) double doped $\text{Sr}_2\text{GdTaO}_6$ samples exhibited two visible emission peaks around 596 and 614 nm, which were assigned to the magnetic and electric dipole transitions ($^5\text{D}_0 \rightarrow ^7\text{F}_1$, $^5\text{D}_0 \rightarrow ^7\text{F}_2$) of europium when excited at 265nm [80, 81]. While Eu(III), Er (III) double doped $\text{Sr}_2\text{GdTaO}_6$ exhibited five distinct visible emission bands around 468nm, 474nm, 584nm, 596nm, and 614nm. These are assigned to the electric transition ($^4\text{F}_{3/2} \rightarrow ^4\text{I}_{15/2}$) of erbium and magnetic and electric dipole transitions ($^5\text{D}_0 \rightarrow ^7\text{F}_1$, $^5\text{D}_0 \rightarrow ^7\text{F}_2$) of europium when excited at 276nm, respectively [82, 83]. The asymmetric ratio is greater than unity (1) for phosphors excited at 276nm, which intimates that Eu^{3+} is displaced at A site in host lattice.

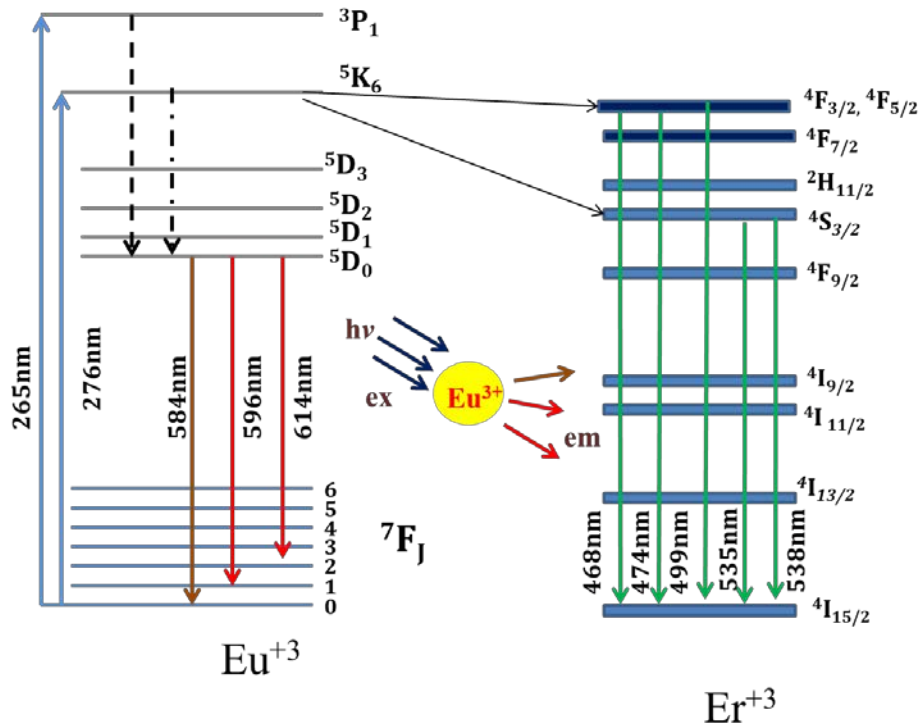


Figure 18 Energy level diagram of Eu(III), Er(III) double doped Sr₂GdTaO₆.

Figure 18 displays an energy level diagram of Eu(III) and Er(III) ion to explain PLE and PL mechanisms. With 265 and 276nm excitation wavelength, electrons jump from the ground state to the excited state. After that, electrons are relaxed to the lowest level ⁵D₀ by using nonradiative transition (NR). In the end, luminescence occurs through the radiative transition ⁵D₀ - ⁷F_j (j = 0, 1, 2).

With the increasing erbium concentration, the color tone of the emanating light shifts from orange to the red region. The results also show that the Eu(III), Er(III) double-doped phosphors herein reported extended further to the latitude of the orange-red tenability region after compared to reported results [84–87]. Moreover, it's good to point out that the combination of the emission color corresponding to coordinate points yields a mixture of light with color in the white-light region possess glow correlated color temperature, i.e., CCT in the 3000K – 6000K range.

References

- [1] A. S. Bhalla, R. Guo, and R. Roy, “The perovskite structure—a review of its role in ceramic science and technology,” *Mater. Res. Innov.*, vol. 4, no. 1, pp. 3–26, Nov. 2000.
- [2] D. Damjanovic, “Piezoelectric properties of perovskite ferroelectrics: unsolved

- problems and future research,” *Ann. Chim. Sci. des Matériaux*, vol. 26, no. 1, pp. 99–106, Feb. 2001.
- [3] N. Nuraje and K. Su, “Perovskite ferroelectric nanomaterials,” *Nanoscale*, vol. 5, no. 19, pp. 8752–8780, 2013.
- [4] M. L. Keith and R. Roy, “Structural relations among double oxides of trivalent elements,” *Am. Miner.*, vol. 39, no. 1/2, pp. 1–23, 1954.
- [5] a. J. Nelson *et al.*, “Electronic structure of lanthanum calcium oxoborate $\text{LaCa}_4\text{O}(\text{BO}_3)_3$,” *J. Electron Spectros. Relat. Phenomena*, vol. 137–140, no. SPEC. ISS., pp. 541–546, Jul. 2004.
- [6] D. Vivien *et al.*, “Overview of the laser and non-linear optical properties of calcium-gadolinium-oxo-borate $\text{Ca}_4\text{GdO}(\text{BO}_3)_3$,” vol. 304, pp. 401–408, 2000.
- [7] E. N. Harvey, “A History of Luminescence From the Earliest Times Until 1900,” *Am. Hist. Rev.*, vol. 44, p. 692, Jul. 1958.
- [8] K. V. R. Murthy and H. S. Virk, “Luminescence Phenomena: An Introduction,” *Defect Diffus. Forum*, vol. 347, pp. 1–34, Dec. 2013.
- [9] B. Valeur and M. N. Berberan-Santos, *Molecular Fluorescence: Principles and Applications*, 2nd ed., vol. 8. Weinheim, Germany: Wiley-VCH Verlag GmbH & Co. KGaA, 2012.
- [10] B. Valeur and M. N. Berberan-Santos, “A brief history of fluorescence and phosphorescence before the emergence of quantum theory,” *Journal of Chemical Education*, vol. 88, no. 6, pp. 731–738, 2011.
- [11] E. M. J. Weber, A. A. Kaminskii, M. J. Weber, M. J. Weber, and M. J. Weber, *PHOSPHOR HANDBOOK*, 2nd ed. FL: CRC Press Taylor & Francis Group 6000 Broken Sound Parkway NW, Suite 300 Boca Raton, FL 33487-2742.
- [12] A. Chmyrov, “Photo-induced dark states in fluorescence spectroscopy – investigations & applications,” KTH, Stockholm, 2010.
- [13] D. L. Dexter, “A theory of sensitized luminescence in solids,” *J. Chem. Phys.*, vol. 21, no. 5, pp. 836–850, 1953.
- [14] A. T. Kozakov *et al.*, “Valence state of cations in manganites $\text{Pr}_{1-x}\text{Ca}_x\text{MnO}_3$ ($0.3 \leq x \leq 0.5$) from X-ray diffraction and X-ray photoelectron spectroscopy,” *J. Alloys Compd.*, vol. 740, pp. 132–142, Apr. 2018.
- [15] J. Mizusaki, “Oxygen nonstoichiometry and defect equilibrium in the perovskite-type oxides $\text{La}_{1-x}\text{Sr}_x\text{MnO}_{3+d}$,” *Solid State Ionics*, vol. 129, no. 1–4, pp. 163–

- 177, Apr. 2000.
- [16] S. Hull, "Superionics: crystal structures and conduction processes," *Reports Prog. Phys.*, vol. 67, no. 7, pp. 1233–1314, Jul. 2004.
- [17] H. LIPSON, "Crystal Structures," *Nature*, vol. 163, no. 4147, pp. 622–622, Apr. 1949.
- [18] P. Kanhere and Z. Chen, "A Review on Visible Light Active Perovskite-Based Photocatalysts," *Molecules*, vol. 19, no. 12, pp. 19995–20022, Dec. 2014.
- [19] T. Saha-Dasgupta, "Double perovskites with 3d and 4d/5d transition metals: compounds with promises," *Mater. Res. Express*, vol. 7, no. 1, p. 014003, Jan. 2020.
- [20] Y. X. Gan, A. H. Jayatissa, Z. Yu, X. Chen, and M. Li, "Hydrothermal Synthesis of Nanomaterials," *J. Nanomater.*, vol. 2020, pp. 1–3, Jan. 2020.
- [21] A. Gysi, Y. Mei, and T. Driesner, "Advances in Numerical Simulations of Hydrothermal Ore Forming Processes," *Geofluids*, vol. 2020, pp. 1–4, Mar. 2020.
- [22] D. Modi, M. S. D. Tawde, S. Garg, D. Khatri, and K. V. R. Murthy, "Photoluminescence Investigation of CdWO₄: Ce, Er doped nano Phosphors," vol. 2, no. I, pp. 9–11, 2012.
- [23] G. W. V. Cave, C. L. Raston, and L. S. Janet, "Recent advances in solventless organic reactions: towards benign synthesis with remarkable versatility," *Chem. Commun.*, pp. 2159–2169, 2001.
- [24] D. Braga and F. Grepioni, "Reactions Between or Within Molecular Crystals," *Angew. Chemie Int. Ed.*, vol. 43, no. 31, pp. 4002–4011, Aug. 2004.
- [25] M. D. Cohen, "The Photochemistry of Organic Solids," *Angew. Chemie Int. Ed. English*, vol. 14, no. 6, pp. 386–393, Jun. 1975.
- [26] M. D. Cohen and G. M. J. Schmidt, "Topochemistry. Part I. A survey," *J. Chem. Soc.*, p. 1996, 1964.
- [27] S. Ekambaram, K. C. Patil, and M. Maaza, "Synthesis of lamp phosphors: facile combustion approach," *J. Alloys Compd.*, vol. 393, no. 1–2, pp. 81–92, May 2005.
- [28] S. T. Aruna and A. S. Mukasyan, "Combustion synthesis and nanomaterials," *Curr. Opin. Solid State Mater. Sci.*, vol. 12, no. 3–4, pp. 44–50, Jun. 2008.
- [29] Y. Xia, B. Gates, Y. Yin, and Y. Lu, "Monodispersed Colloidal Spheres: Old Materials with New Applications," *Adv. Mater.*, vol. 12, no. 10, pp. 693–713, May 2000.
- [30] N. Kunkel, A. D. Sontakke, S. Kohaut, B. Viana, and P. Dorenbos, "Thermally

- Stimulated Luminescence and First-Principle Study of Defect Configurations in the Perovskite-Type Hydrides $\text{LiMH}_3:\text{Eu}^{2+}$ ($M = \text{Sr}, \text{Ba}$) and the Corresponding Deuterides,” *J. Phys. Chem. C*, vol. 120, no. 51, pp. 29414–29422, Dec. 2016.
- [31] B. Ghosh, A. Dutta, and T. P. Sinha, “Vibrational modes and electrical transport in $\text{Sr}_2\text{GdTaO}_6$,” *Mater. Chem. Phys.*, vol. 143, no. 1, pp. 26–33, Dec. 2013.
- [32] A. Dutta and T. P. Sinha, “Dielectric Relaxation and Electronic Structure of Double Perovskite $\text{Ca}_2\text{AlNbO}_6$,” *Integr. Ferroelectr.*, vol. 116, no. July 2015, pp. 41–50, 2010.
- [33] C. Suryanarayana and M. G. Norton, *X-Ray Diffraction*, 1st ed. Boston, MA: Springer US, 1998.
- [34] M. Licheron, F. Gervais, J. Coutures, and J. Choisnet, “‘ Ba_2BiO_4 ’ surprisingly found as a cubic double perovskite,” *Solid State Commun.*, vol. 75, no. 9, pp. 759–763, Sep. 1990.
- [35] A. E. Lavat and E. J. Baran, “IR-spectroscopic characterization of $\text{A}_2\text{BB}_0\text{O}_6$ perovskites,” vol. 32, pp. 167–174, 2003.
- [36] L. Guerbous and A. Boukerika, “Nanomaterial Host Bands Effect on the Photoluminescence Properties of Ce-Doped YAG Nanophosphor Synthesized by Sol-Gel Method,” *J. Nanomater.*, vol. 2015, pp. 1–10, 2015.
- [37] V. M. Goldschmidt, “Die Gesetze der Krystallochemie,” *Naturwissenschaften*, vol. 14, no. 21, pp. 477–485, 1926.
- [38] R. D. Shannon, “Revised effective ionic radii and systematic studies of interatomic distances in halides and chalcogenides,” *Acta Crystallogr. Sect. A*, vol. 32, no. 5, pp. 751–767, Sep. 1976.
- [39] M. W. Lufaso and P. M. Woodward, “Prediction of the crystal structures of perovskites using the software program SPuDS,” *Acta Crystallogr. Sect. B*, vol. 57, no. 6, pp. 725–738, 2001.
- [40] R. K. Tamrakar, D. P. Bisen, C. S. Robinson, I. P. Sahu, and N. Brahme, “Ytterbium Doped Gadolinium Oxide ($\text{Gd}_2\text{O}_3:\text{Yb}^{3+}$) Phosphor: Topology, Morphology, and Luminescence Behaviour,” *Indian J. Mater. Sci.*, vol. 2014, pp. 1–7, 2014.
- [41] R. K. Tamrakar, D. P. Bisen, and N. Brahme, “Comparison of photoluminescence properties of Gd_2O_3 phosphor synthesized by combustion and solid state reaction method,” *J. Radiat. Res. Appl. Sci.*, vol. 7, no. 4, pp. 550–559, Oct. 2014.
- [42] A. García-Murillo *et al.*, “Elaboration and scintillation properties of Eu^{3+} -doped

- Gd₂O₃ and Lu₂O₃ sol–gel films,” *Nucl. Instruments Methods Phys. Res. Sect. A Accel. Spectrometers, Detect. Assoc. Equip.*, vol. 486, no. 1–2, pp. 181–185, Jun. 2002.
- [43] G. Blasse and B. C. Grabmaier, *Luminescent Materials*. Berlin, Heidelberg: Springer Berlin Heidelberg, 1994.
- [44] K. V. Dabre, K. Park, and S. J. Dhoble, “Synthesis and photoluminescence properties of microcrystalline Sr₂ZnWO₆:RE³⁺ (RE = Eu, Dy, Sm and Pr) phosphors,” *J. Alloys Compd.*, vol. 617, pp. 129–134, Dec. 2014.
- [45] F. M. Emen and R. Altinkaya, “Luminescence and thermoluminescence properties of Sr₃WO₆:Eu³⁺ phosphor,” *J. Lumin.*, vol. 134, pp. 618–621, Feb. 2013.
- [46] S. Zhang, Y. Hu, L. Chen, X. Wang, G. Ju, and Y. Fan, “Photoluminescence properties of Ca₃WO₆:Eu³⁺ red phosphor,” *J. Lumin.*, vol. 142, pp. 116–121, Oct. 2013.
- [47] W. F. Zhang, Z. Yin, M. S. Zhang, Z. L. Du, and W. C. Chen, “Roles of defects and grain sizes in photoluminescence of nanocrystalline SrTiO₃,” *J. Phys. Condens. Matter*, vol. 11, no. 29, pp. 5655–5660, Jul. 1999.
- [48] X. Zhao, Y. Ding, Z. Li, T. Yu, and Z. Zou, “An efficient charge compensated red phosphor Sr₃WO₆: K⁺, Eu³⁺ – For white LEDs,” *J. Alloys Compd.*, vol. 553, pp. 221–224, Mar. 2013.
- [49] X. Zhao *et al.*, “Efficient red phosphor double-perovskite Ca₃WO₆ with A-site substitution of Eu³⁺,” *Dalt. Trans.*, vol. 42, no. 37, p. 13502, 2013.
- [50] R. Jacob and I. Jayakumari, “X-ray diffraction line profile analysis of Ba Sr_{0.6} Fe_{0.4} TiO₃ (BSFTO),” *Int. J. Chem. Stud.*, vol. 5, no. 2, pp. 12–21, 2015.
- [51] M. T. Anderson and K. R. Poeppelmeier, “Lanthanum copper tin oxide (La₂CuSnO₆): a new perovskite-related compound with an unusual arrangement of B cations,” *Chem. Mater.*, vol. 3, no. 3, pp. 476–482, May 1991.
- [52] J. E. Yoo and J. Choi, “Surfactant-assisted growth of anodic nanoporous niobium oxide with a grained surface,” *Electrochim. Acta*, vol. 55, no. 18, pp. 5142–5147, Jul. 2010.
- [53] Y. Huang, T. Wei, and Y. Ge, “Preparation and characterization of novel Ce(III)-gelatin complex,” *J. Appl. Polym. Sci.*, vol. 108, no. 6, pp. 3804–3807, Jun. 2008.
- [54] J. LIN *et al.*, “Crystallization of TeO₂–Nb₂O₅ glasses and their network structural evolution,” *Mater. Sci.*, vol. 27, p. 329, 2009.
- [55] K. Binnemans, “Interpretation of europium(III) spectra,” *Coord. Chem. Rev.*, vol.

- 295, pp. 1–45, Jul. 2015.
- [56] K. H. Hellwege and H. G. Kahle, “Spektrum und Struktur kristalliner Europiumsalze. I. Europiumchlorid $\text{EuCl}_2 \cdot 6 \text{H}_2\text{O}$,” *Zeitschrift für Phys.*, vol. 129, no. 1, pp. 62–84, Jan. 1951.
- [57] K. H. Hellwege and H. G. Kahle, “Spectrum and structure of crystalline europium salts II. Europium bromat $\text{Eu}(\text{BrO}_3)_3 \cdot 9\text{H}_2\text{O}$,” *Zeitschrift für Phys.*, vol. 129, no. 1, pp. 85–103, Jan. 1951.
- [58] R. Rajaramakrishna, P. Nijapai, P. Kidkhunthod, H. J. Kim, J. Kaewkhao, and Y. Ruangtaweep, “Molecular dynamics simulation and luminescence properties of Eu^{3+} doped molybdenum gadolinium borate glasses for red emission,” *J. Alloys Compd.*, vol. 813, p. 151914, Jan. 2020.
- [59] S. Som, A. Choubey, and S. K. Sharma, “Spectral and trapping parameters of Eu^{3+} in $\text{Gd}_2\text{O}_2\text{S}$ nanophosphor,” *J. Exp. Nanosci.*, vol. 10, no. 5, pp. 350–370, Mar. 2015.
- [60] N. Pathak, S. Mukherjee, D. Das, D. Dutta, S. Dash, and R. M. Kadam, “Evolution of different defect clusters in Eu^{3+} doped KMgF_3 and Eu^{3+} , Li^+ co-doped KMgF_3 compounds and the immediate impact on the phosphor characteristics,” *J. Mater. Chem. C*, 2020.
- [61] Y. Shimada, H. Kiyama, and Y. Tokura, “Magnetoelectric emission in rare-earth doped ferroelectric crystals $\text{La}_2\text{Ti}_2\text{O}_7:\text{R}^{3+}$ ($\text{R}=\text{Er}$, Eu , and Nd),” *Phys. Rev. B*, vol. 75, no. 24, p. 245125, Jun. 2007.
- [62] G. B. F. Bosco and L. R. Tessler, “Crystal field parameters of the C2 site in Eu_2O_3 ,” *Opt. Mater. X*, vol. 2, p. 100028, May 2019.
- [63] E. Climent-pascual, R. Ruiz-bustos, and R. Sa, “Non-collinear magnetic structure of the $\text{Sr}_2\text{ErRuO}_6$ double perovskite,” *Prog. Solid State Chem.*, vol. 35, no. 2–4, pp. 211–219, 2007.
- [64] D. Yoshihiro and H. Yukio, “Crystal structures and magnetic properties of ordered perovskites $\text{Sr}_2\text{LnRuO}_6$ ($\text{Ln} = \text{Eu-Lu}$),” *J. Phys. Condens. Matter*, vol. 11, no. 25, pp. 4813–4820, 1999.
- [65] B. D. Cullity, *Elements of X-Ray Diffraction*, 1st ed. MASSACHUSETTS: ADDISON-WESLEY PUBLISHING COMPANY, Inc., 1956.
- [66] M. Srinivas, D. Modi, N. Patel, V. Verma, and K. V. R. Murthy, “Photoluminescence Studies and Core–Shell Model Approach for Rare Earthdoped CdWO_4 Nano Phosphor,” *J. Inorg. Organomet. Polym. Mater.*, vol.

- 24, no. 6, pp. 988–993, Nov. 2014.
- [67] R. Ratheesh, H. Sreemoolanadhan, and M. T. Sebastian, “Vibrational Analysis of $Ba_{5-x}Sr_xNb_4O_{15}$ Microwave Dielectric Ceramic Resonators,” *Solid State Chem.*, vol. 8, no. 131, pp. 2–8, 1997.
- [68] L. J. T., “Infrared-Absorption Studies on Barium Titanate and Related Materials,” *Phys. Rev.*, vol. 105, p. 1740, 1957.
- [69] B. E.J., “Structural chemistry and physicochemical properties of perovskite-like materials,” *Catal. Today*, vol. 8, no. 2, pp. 133–151, 1990.
- [70] S. D. Ross, *Inorganic infrared and Raman spectra*. London; New York: McGraw-Hill, 1972.
- [71] A. E. Lavat, M. C. Grasselli, E. J. Baran, and R. C. Mercader, “Spectroscopic characterization of $BaLnSnO$ materials: 2 5.5 ceramic substrates for high T superconductors,” *Mater. Letters*, vol. 47, no. 4–5, pp. 194–198, 2001.
- [72] P. Z. Zambare, A. P. Zambare, K. V. R. Murthy, and O. H. Mahajan, “Research Article Synthesis and Characterization of Red Emitting $Sr_2CeO_4:Eu^{3+}$ Nano Phosphors,” *J. Chem. Pharm. Res.*, vol. 4, no. 4, pp. 1990–1994, 2012.
- [73] E. Orhan *et al.*, “Room-temperature photoluminescence of $BaTiO_3$: Joint experimental and theoretical study,” *Phys. Rev. B*, vol. 71, no. 8, p. 085113, Feb. 2005.
- [74] Y. Kawabe *et al.*, “Photoluminescence of perovskite lanthanum aluminate single crystals,” *J. Appl. Phys.*, vol. 87, no. 10, pp. 7594–7596, May 2000.
- [75] H. Mizoguchi, P. M. Woodward, C.-H. Park, and D. A. Keszler, “Strong Near-Infrared Luminescence in $BaSnO_3$,” *J. Am. Chem. Soc.*, vol. 126, no. 31, pp. 9796–9800, Aug. 2004.
- [76] R. Leonelli and J. L. Brebner, “Time-resolved spectroscopy of the visible emission band in strontium titanate,” *Phys. Rev. B*, vol. 33, no. 12, pp. 8649–8656, Jun. 1986.
- [77] H. E. Hoefdraad, “The charge-transfer absorption band of Eu^{3+} in oxides,” *J. Solid State Chem.*, vol. 15, no. 2, pp. 175–177, Oct. 1975.
- [78] V. Sivakumar and U. V. Varadaraju, “Synthesis, phase transition and photoluminescence studies on Eu^{3+} -substituted double perovskites—A novel orange-red phosphor for solid-state lighting,” *J. Solid State Chem.*, vol. 181, no. 12, pp. 3344–3351, Dec. 2008.
- [79] Y. Zhang, J. Xu, Q. Cui, and B. Yang, “ Eu^{3+} -doped $Bi_4Si_3O_{12}$ red phosphor for

- solid state lighting: microwave synthesis, characterization, photoluminescence properties and thermal quenching mechanisms,” *Sci. Rep.*, vol. 7, no. 1, p. 42464, Mar. 2017.
- [80] Ravina *et al.*, “Judd-Ofelt Itemization and Influence of Energy Transfer on Sm³⁺ ions Activated B₂O₃-ZnF₂-SrO-SiO₂ Glasses for Orange-Red Emitting Devices,” *J. Lumin.*, p. 117651, Sep. 2020.
- [81] P. Dorenbos, “The Eu³⁺ charge transfer energy and the relation with the band gap of compounds,” *J. Lumin.*, vol. 111, no. 1–2, pp. 89–104, Jan. 2005.
- [82] X. Yu *et al.*, “Near infrared to visible upconversion emission in Er³⁺/Yb³⁺ co-doped NaGd(WO₄)₂ nanoparticles obtained by hydrothermal method,” *J. Lumin.*, vol. 154, pp. 111–115, Oct. 2014.
- [83] G.-C. Yi, B. A. Block, G. M. Ford, and B. W. Wessels, “Luminescence quenching in Er-doped BaTiO₃ thin films,” *Appl. Phys. Lett.*, vol. 73, no. 12, pp. 1625–1627, Sep. 1998.
- [84] N. Jain *et al.*, “Synthesis and Rational design of Europium and Lithium Doped Sodium Zinc Molybdate with Red Emission for Optical Imaging,” *Sci. Rep.*, vol. 9, no. 1, p. 2472, Dec. 2019.
- [85] Y. Gao *et al.*, “Tb³⁺ and Eu³⁺ co-doped Ba₆Bi₉B₇₉O₁₃₈: color-tunable phosphors by utilizing the host-sensitization effect of Bi³⁺ and enhancement of red emission upon heating,” *New J. Chem.*, vol. 41, no. 5, pp. 2037–2045, 2017.
- [86] A. Katelnikovas, H. Winkler, A. Kareiva, and T. Jüstel, “Synthesis and optical properties of green to orange tunable garnet phosphors for pcLEDs,” *Opt. Mater. (Amst.)*, vol. 33, no. 7, pp. 992–995, May 2011.
- [87] D. Chen, Y. Wang, Y. Yu, P. Huang, and F. Weng, “Novel rare earth ions-doped oxyfluoride nano-composite with efficient upconversion white-light emission,” *J. Solid State Chem.*, vol. 181, no. 10, pp. 2763–2767, Oct. 2008.